Nano-Micro Letters

ISSN 2311-6706
e-ISSN 2150-5551
CN 31-2103/TB

ARTICLE

https://doi.org/10.1007/s40820-020-00445-x

Cite as
Nano-Micro Lett.
(2020) 12:110

Received: 29 February 2020
Accepted: 11 April 2020


# High-Performance Aqueous Zinc–Manganese Battery with Reversible $Mn^{2+}/Mn^{4+}$ Double Redox Achieved by Carbon Coated $MnO_x$ Nanoparticles

Jingdong Huang[1], Jing Zeng[1], Kunjie Zhu[2], Ruizhi Zhang[3] ✉, Jun Liu[1] ✉

Jingdong Huang and Jing Zeng contributed equally to this work.

✉ Ruizhi Zhang, zhangruizhi@gmail.com; Jun Liu, liujun4982004@csu.edu.cn

[1] School of Materials Science and Engineering, Central South University, Changsha 410083, People's Republic of China

[2] Key Laboratory of Advanced Energy Materials Chemistry (Ministry of Education), College of Chemistry, Nankai University, Tianjin 300071, People's Republic of China

[3] Hunan Institute of Technology, Hengyang 421002, People's Republic of China

## HIGHLIGHTS

- Aqueous zinc-manganese batteries with reversible $Mn^{2+}/Mn^{4+}$ double redox are achieved by carbon-coated $MnO_x$ nanoparticles.
- Combined with $Mn^{2+}$-containing electrolyte, the $MnO_x$ cathode achieves an ultrahigh energy density with a peak of 845.1 Wh $kg^{-1}$ and an ultralong lifespan of 1500 cycles.
- The electrode behaviors and reaction mechanism are systematically discussed by combining electrochemical measurements and material characterization.

**ABSTRACT** There is an urgent need for low-cost, high-energy-density, environmentally friendly energy storage devices to fulfill the rapidly increasing need for electrical energy storage. Multi-electron redox is considerably crucial for the development of high-energy-density cathodes. Here we present high-performance aqueous zinc–manganese batteries with reversible $Mn^{2+}/Mn^{4+}$ double redox. The active $Mn^{4+}$ is generated in situ from the $Mn^{2+}$-containing $MnO_x$ nanoparticles and electrolyte. Benefitting from the low crystallinity of the birnessite-type $MnO_2$ as well as the electrolyte with $Mn^{2+}$ additive, the $MnO_x$ cathode achieves an ultrahigh energy density with a peak of 845.1 Wh $kg^{-1}$ and an ultralong lifespan of 1500 cycles. The combination of electrochemical measurements and material characterization reveals the reversible $Mn^{2+}/Mn^{4+}$ double redox (birnessite-type $MnO_2 \leftrightarrow$ monoclinic MnOOH and spinel $ZnMn_2O_4 \leftrightarrow Mn^{2+}$ ions). The reversible $Mn^{2+}/Mn^{4+}$ double redox electrode reaction mechanism offers new opportunities for the design of low-cost, high-energy-density cathodes for advanced rechargeable aqueous batteries.

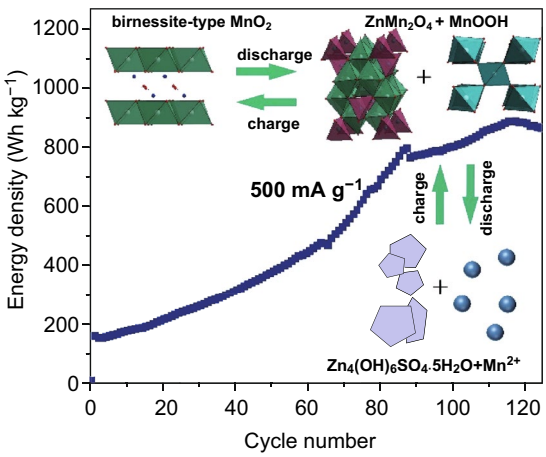


**KEYWORDS** Aqueous zinc–manganese batteries; Mn-based cathode materials; High energy density; $Mn^{2+}/Mn^{4+}$ double redox

Published online: 13 May 2020

## 1 Introduction

Considering the projected climatic deterioration, pollution, and inherent limit of fossil fuels, focus toward more environmentally friendly and sustainable energy sources continues to grow [1, 2]. Nevertheless, the utilization of sustainable energy sources such as solar, water, and wind requires a safe, efficient, and economic energy conversion system that can smoothen the intermittency of sustainable energy [3]. Although current lithium-ion batteries (LIBs) have dominated the portable energy market, their large-scale grid application is limited by the high cost and scarcity of Li resources and safety concerns associated with flammable organic electrolytes that lead to thermal runaway [4–6]. Recently, rechargeable aqueous zinc-based batteries have been considered candidates for stationary grid-level storage of the intermittent renewable energies due to their low cost, improved safety, simpler manufacturing conditions, and greener operation [7, 8].

As for the low cost, non-toxicity, and high theoretical capacity, Mn-based materials are considered as ideal cathode materials for aqueous zinc-ion batteries (AZIBs) [9, 10]. Current studies focus on crystallographic tunnel-type structures $MnO_2$, including α-$MnO_2$, β-$MnO_2$, γ-$MnO_2$, and other types [11–16]. Additionally, spinel-type $Mn_3O_4$ and $ZnMn_2O_4$ show as viable cathode materials for AZIBs [17–20]. Recently, due to its larger capacity and higher metal ion diffusion rate, layered $MnO_2$ is considered to be a more promising cathode material [21]. However, most of the $MnO_2$ that has been reported only utilizes the electron during $Mn^{4+}/Mn^{3+}$ conversion, therefore those cathode materials fall short of meeting the demands for portable and large-scale stationary energy storage systems. The $Mn^{2+}/Mn^{4+}$ double redox is observed in the tunnel-type γ-$MnO_2$ [22]. During the discharge process, spinel-type $ZnMn_2O_4$, tunnel-type γ-$Zn_xMn^{2+}O_2$, and layered-type L-$Zn_yMn^{2+}O_2$ are generated in sequence, and a high capacity of 285 mAh $g^{-1}$ can be achieved. The structural variation is reversible, but the tunnel-type γ-$MnO_2$ suffers from poor electrical and ionic conductivities [23]. Therefore, it is still highly infusive to discover potential satisfactory Mn-based cathode materials for energy storage.

Herein, we propose the use of carbon-coated $MnO_x$ nanoparticles as a cathode material for zinc–manganese batteries. In these batteries, the active low-crystallinity birnessite-type $MnO_2$ is generated in situ from the $Mn^{2+}$-containing $MnO_x$ nanoparticles and electrolyte during the charge process. Owing to the lower crystallinity, the active birnessite-type $MnO_2$ contains higher energy and possesses the ability to achieve $Mn^{2+}/Mn^{4+}$ double redox [24]. In addition, the small particle size of $MnO_x$ and the high conductivity of the carbon substrates provide good conditions for the oxidation reactions. Benefitting from the $Mn^{2+}/Mn^{4+}$ double redox, the $MnO_x$ cathode using $Mn^{2+}$-containing $ZnSO_4$ electrolyte exhibits an ultrahigh energy density with a peak of 845.1 Wh $kg^{-1}$ and an ultralong lifespan of 1500 cycles. A detailed investigation is also performed to analyze the mechanism of the reversible $Mn^{2+}/Mn^{4+}$ double redox. This working principle of the zinc–manganese battery is illustrated in Fig. 1a. These findings may offer new opportunities to design low-cost and high-performance aqueous zinc–manganese batteries for large-scale energy storage.

## 2 Experimental Section

### 2.1 Synthesis of α-$MnO_2$

The α-$MnhO_2$ was synthesized using a hydrothermal procedure [25]. Firstly, $KMnO_4$ (0.7 g) was dissolved in deionized water (70 mL); then, concentrated HCl (3.3 mL) was added into the solution under continuous vigorous stirring at room temperature for 10 min. The final solution was transferred into a Teflon-lined stainless-steel autoclave (100 mL) and maintained at 140 °C for 16 h. Next, the brown product was collected by centrifugation and washed with deionized water and ethanol for three times. Finally, the brown product was dried at 70 °C for 24 h.

### 2.2 Synthesis of $MnO_x$ and MnO

In a typical procedure, α-$MnO_2$ nanorods (0.04 g) were dispersed in ethanol (10 mL) with 2-methylimidazole (2 g) dissolved. The obtained suspension was dried in a drying oven at 80 °C for 24 h. Then the dried sample was carefully ground by agate mortar. After that, the powders were heated at 700 °C for 1, 2, or 3 h at a rate of 2 °C $min^{-1}$ in a tube furnace under a flowing Ar atmosphere to obtain


https://doi.org/10.1007/s40820-020-00445-x

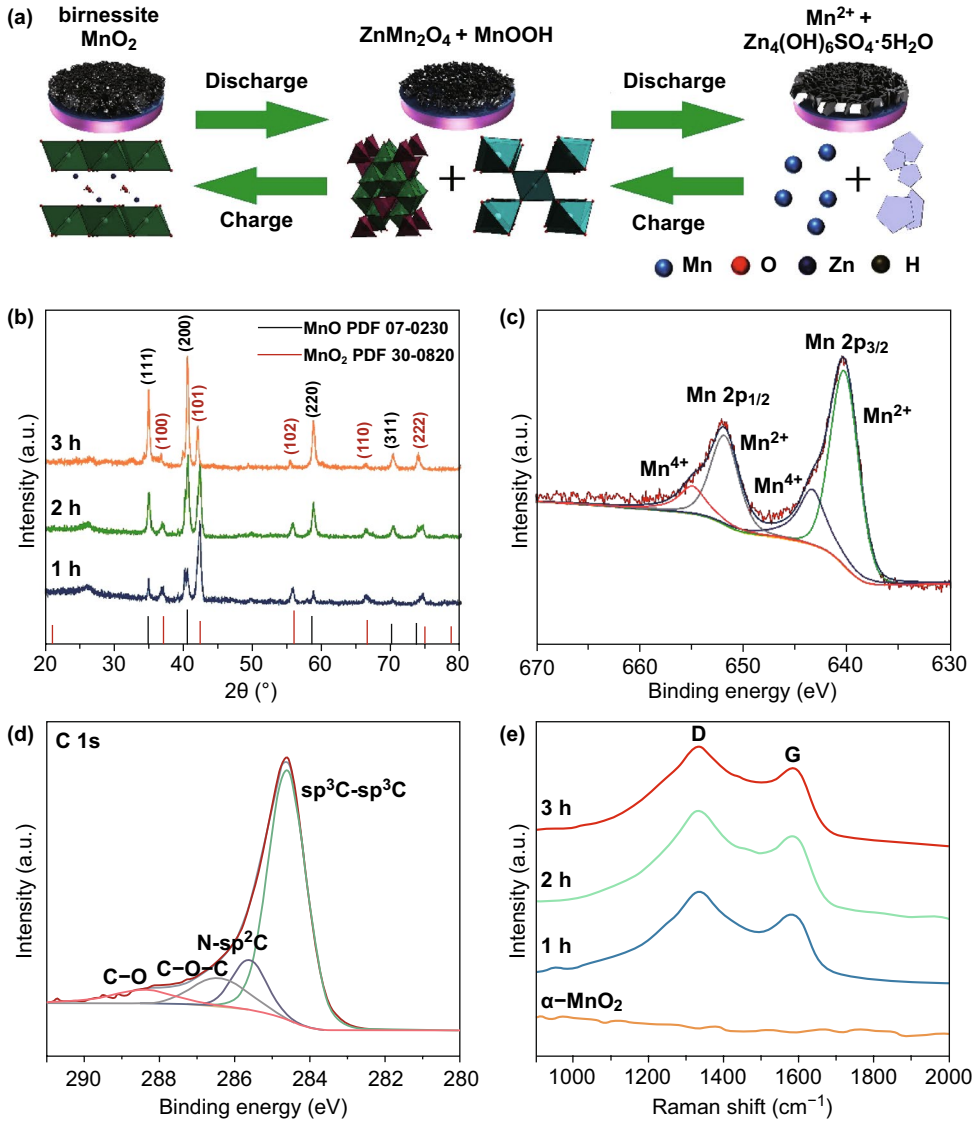


**Fig. 1** **a** Working principle of Zn/$MnO_x$ battery. **b** XRD patterns of $MnO_x$. XPS spectra of $MnO_x$-2: **c** high resolution of Mn 2*p* and **d** high resolution of C 1*s*. **e** Raman spectra of the $MnO_x$ and α-$MnO_2$

$MnO_x$-1, $MnO_x$-2, or $MnO_x$-3. Besides, the MnO was obtained by heating the brown powders at 700 °C for 2 h at a rate of 2 °C $min^{-1}$ in a tube furnace under a flowing $Ar/H_2$ atmosphere.

### 2.3 Materials Characterization

X-ray diffraction (XRD) measurements were performed on a Rigaku D/max 2500 powder diffractometer with monochromatic Cu-Kα radiation and the wavelength of 1.54178 Å. SEM and transmission electron microscope (TEM) images were taken using a FEI Helios Nanolab G3 UC and TEM JEOLJEM-2100 electron microscope, respectively. The elementary composition and valence state of samples were characterized by X-ray photoelectron spectroscope (XPS, Thermo ESCALAB 250Xi, monochromatic Al-Kα radiation). Raman spectra were collected on an Invia Raman spectrometer, using an excitation laser of 514.5 nm. ICP-OES spectrometer (SPECTRO BLUE SOP) was carried out to determine the concentration of Mn and S elements.

### 2.4 Electrochemical Measurements

The electrochemical measurements were tested by assembly of CR2032-type coin cells in air atmosphere. The working electrode film was prepared by coating the slurry on a Ti foil, and the slurry consisted with active materials, polyvinylidene fluoride (PVDF) binder, super P additive (7: 2: 1). The mass loading of active materials is around 1.5 mg $cm^{-2}$. Zn foil was used as the counter electrode. 1 M $ZnSO_4$ and 0.3 M $MnSO_4$ solution were used as electrolyte. Cyclic voltammetry (CV) curves were recorded on an electrochemical workstation (CHI660E). The galvanostatic discharge–charge tests were performed on a Land CT 2001A tester in a potential window of 0.8–1.8 V.

## 3 Results and Discussion

### 3.1 Structural Characterization

The crystallographic structure and the phase composition of the pre-reduced $MnO_x$ are examined by XRD measurement. As shown in Fig. 1b, the diffraction peaks of manganese oxides indicate a crystalline hybrid, which match well with simulated $MnO_2$ (JCPDS Card No. 30-0820) and MnO (JCPDS Card No. 07-0230). The XRD results clearly show that the ratios of MnO to $MnO_2$ in the products calcined at different reaction time are completely different. The synthesized manganese oxides are labeled $MnO_x$-1, $MnO_x$-2, and $MnO_x$-3, respectively. The XRD analysis of the α-$MnO_2$ and MnO is also shown in Fig. S1a, b.

In order to further analyze the manganese valence states of $MnO_x$ and α-$MnO_2$, the samples were analyzed by X-ray photoelectron spectroscopy (XPS) (Figs. 1c, d, S2). The high-resolution XPS spectrum of Mn 2*p* for $MnO_x$ composite displays four peaks with binding energies at 640.35 eV (651.92 eV) and 643.50 eV (654.92 eV), which correspond to $Mn^{2+}$ and $Mn^{4+}$, respectively [26]. This result further proves that the pre-reduced $MnO_x$ is a composite of $MnO_2$ and MnO. For $MnO_x$-1, $MnO_x$-2, and $MnO_x$-3, the fractions of $Mn^{2+}$ are ≈64.1%, 71.4%, and 79.3%, respectively. As shown in Fig. 1d, the high-resolution XPS spectrum of C 1 *s* for $MnO_x$ composite can be fitted into four parts, including the peaks located at 288.4, 286.5, 285.5, and 284.5 eV, corresponding to C–O, C–O–C, N–$sp^2$C, and $sp^3$C–$sp^3$C bonds, respectively [27]. The Raman spectrum is given in Fig. 1e. The broad peaks located at 1332 and 1586 $cm^{-1}$ are related

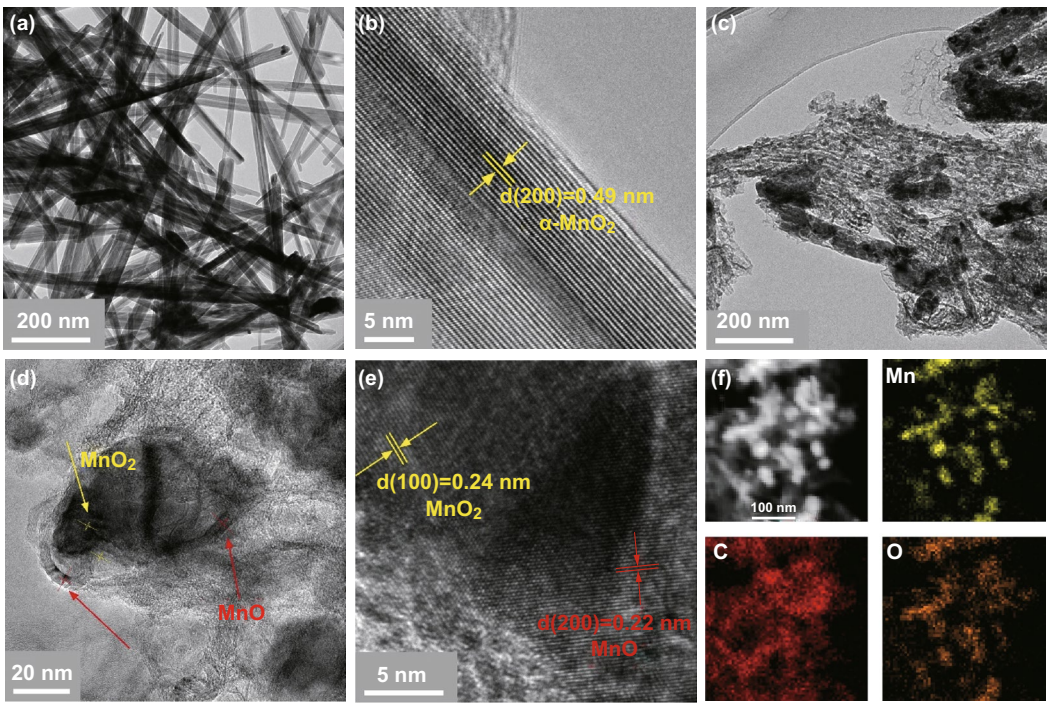


**Fig. 2** **a** TEM and **b** HRTEM images of α-$MnO_2$. **c** TEM image, **d, e** HRTEM images, and **f** EDX elemental mapping images of $MnO_x$-2


https://doi.org/10.1007/s40820-020-00445-x

to the D band and G band of carbon, respectively. The high intensity of the D band indicates the presence of defects and non-graphitic carbon in the carbon coating [28].

The morphology of as-prepared α-$MnO_2$ precursors is assessed by TEM, showing a nanorod shape for α-$MnO_2$ (Fig. 2a). The high-resolution (HR) TEM image (Fig. 2b) possesses regular lattice fringes with *d*-spacing of 0.49 nm, corresponding to the interplanar distance of (200) plane of α-$MnO_2$. After the composite powder is calcined, the morphology of α-$MnO_2$ changes to smaller nanoparticles coated with carbon (Fig. 2c). The $MnO_x$ nanoparticles are highly dispersed in the carbon substrate and form better contact with the electrolyte, thereby establishing a highly conductive network for the electrons and further providing good conditions for the oxidation reaction of $MnO_x$ and $Mn^{2+}$ ions [29]. HRTEM images (Fig. 2d, e) reveal that $MnO_x$ possesses regular lattice fringes spacing of 0.24 and 0.22 nm, corresponding to (100) plane of $MnO_2$, and (200) plane of MnO, respectively. The high-angle annular dark-field (HAADF)-STEM image and energy-dispersive X-ray (EDX) elemental mapping images (Fig. 2f) of $MnO_x$ confirm the dispersion of small $MnO_x$ nanoparticles in the carbon coating.

### 3.2 Electrochemical Characterization

Figure 3a compares cycling performance between $MnO_x$-2 and α-$MnO_2$ cathodes at 0.2 A $g^{-1}$. Drastic capacity fade can be clearly seen in the curves of α-$MnO_2$, maintaining 154.5 mAh $g^{-1}$ after 75 cycles. With respect to $MnO_x$-2 electrode, the initial charge capacity is 156.3 mAh $g^{-1}$ due to the electrochemical oxidation of $Mn^{2+}$. After 75 cycles, the $MnO_x$-2 electrode achieves specific capacity up to 714.7 mAh $g^{-1}$ (based on the active material initial mass of cathode). The capacity of $MnO_x$-2 exceeding its theoretical capacity can be attributed to the addition of $Mn^{2+}$ in the electrolyte. The $Mn^{2+}$ added in the electrolyte can also participate in the reversible $Mn^{2+}/Mn^{4+}$ double redox, so the capacity of $MnO_x$-2 tops its theoretical capacity. In addition, $MnO_x$-2 cathode displays a gradually increasing of specific capacity, possibly due to the following reason: The MnO in the $MnO_x$ is gradually oxidized during each charging process. And the newly formed $MnO_2$ can also achieve reversible $Mn^{2+}/Mn^{4+}$ double redox to increase the specific capacity. This phenomenon is commonly observed in transition metal oxides [30, 31]. The voltage profiles of $MnO_x$-2 are shown in Fig. S6. As shown in Fig. S6, the voltage profiles of this electrode do not change significantly in the first 50 cycles. During the capacity decay, however, there are some changes in the voltage profiles of the electrode, which may be due to changes of electrode materials.

As shown in Fig. 3b, the $MnO_x$-2 electrode using $Mn^{2+}$-containing electrolyte exhibits an ultrahigh energy density with a peak of 845.1 Wh $kg^{-1}$ at 500 mA $g^{-1}$. Furthermore, the rate capabilities are compared at increased current densities (Fig. 3c). The $MnO_x$ electrode exhibits capacities of 844.5 mAh $g^{-1}$ at 0.1 A $g^{-1}$ after 10 cycles. As currents increase from 0.1 to 1.5 A $g^{-1}$, for $MnO_x$ electrode, capacities of 844.5, 783.6, 551.1, 226.8, 114.8, and 59.7 mAh $g^{-1}$ are delivered. For comparison, the α-$MnO_2$ electrode fades drastically from 270.7 (0.1 A $g^{-1}$) to 27.2 mAh $g^{-1}$ (1.5 A $g^{-1}$). Upon rate recovery to 0.2 A $g^{-1}$, a reversible capacity of 863 mAh $g^{-1}$ is restored for $MnO_x$ electrode. Moreover, the $MnO_x$ electrode displays higher energy density (1158 Wh $kg^{-1}$) and power density (1212 W $kg^{-1}$) in the Ragone plot in comparison with α-$MnO_2$ cathode for aqueous ZIBs as shown in Fig. 3d. When the $MnO_x$ is cycled 1500 times at a high rate of 1 A $g^{-1}$, a capacity of 133.3 mAh $g^{-1}$ is maintained (Fig. 3e). It is evident that $MnO_x$ displays greater stability and reversibility than α-$MnO_2$ during charging/discharging. Under different current densities, the electrochemical properties of manganese oxides, such as initial specific capacity, maximum specific capacity, and activation process, are different. These phenomena may be due to the different polarizations of the electrodes at different current densities. As compared with most Mn-based Zn-ion batteries (Table S1), the carbon-coated $MnO_x$ cathode using $Mn^{2+}$-containing electrolyte delivers competitive energy density. The electrochemical performances of $MnO_x$-1, $MnO_x$-3, and MnO are provided in Figs. S3–S5.

### 3.3 Reaction Mechanism

In order to understand the reasons for the superior electrochemical performance of carbon-coated $MnO_x$ nanoparticles, the ex situ SEM, ex situ XRD, ex situ XPS, and ex situ inductively coupled plasma optical emission spectroscopy (ICP-OES) at different cycling states were conducted to reveal the morphology and crystal structure evolution of the $MnO_x$ cathode. Figure 4 shows the ex situ SEM images of the $MnO_x$-2 cathode materials at different cycling stages.

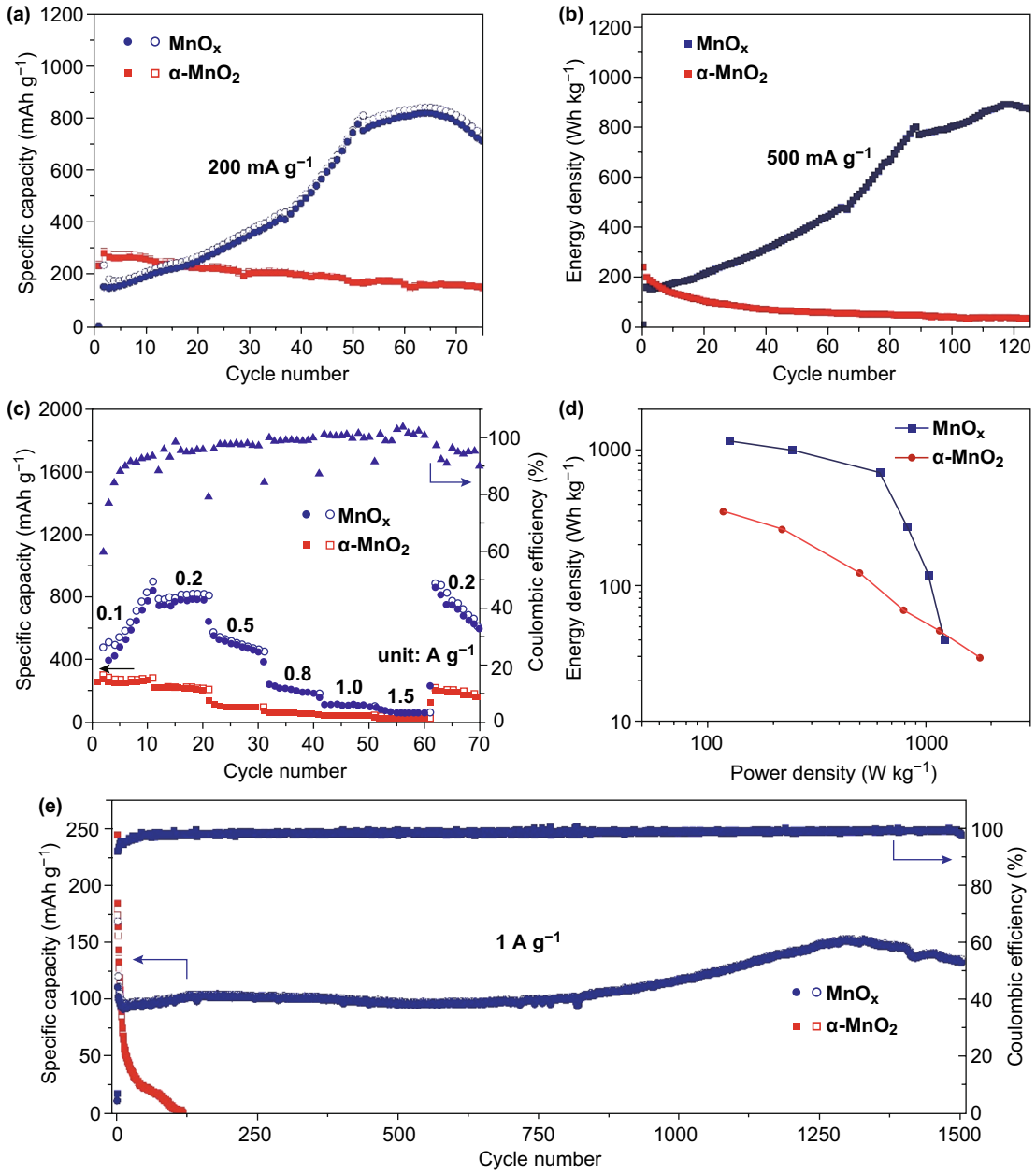


**Fig. 3** Cycling performance of $MnO_x$-2 and α-$MnO_2$ **a** at 0.2 A $g^{-1}$ and **b** at 0.5 A $g^{-1}$. **c** Rate performance of $MnO_x$-2 and α-$MnO_2$. **d** Ragone plot and **e** long cycling performances at 1.0 A $g^{-1}$ of $MnO_x$-2 and α-$MnO_2$ cathode

As shown in Fig. 4a, the nanosheet array covers the electrode surface when discharging to 1.28 V. But the nanosheet array structure disappears and the electrode surface is covered by new flake-like compounds in the fully discharged stage (Fig. 4b). When charging to 1.55 V (Fig. 4c), the nanosheet arrays are regenerated. And thicker active materials with nanosheet structure are generated on the electrode surface in the fully charged stage (Fig. 4d). The nanosheet-like structure formed in situ during the charge process possesses a high specific surface area, which can facilitate electron transport and shorten the ion diffusion length. The EDX elemental (Mn, Zn, and O) mapping images at different charged/discharge states are shown in Figs. 4e, f, and S7, S8. At the fully charged state, the electrodes are covered with nanosheets, and Mn and O elements are distributed on the nanosheets, but there is almost no Zn element. On the


https://doi.org/10.1007/s40820-020-00445-x

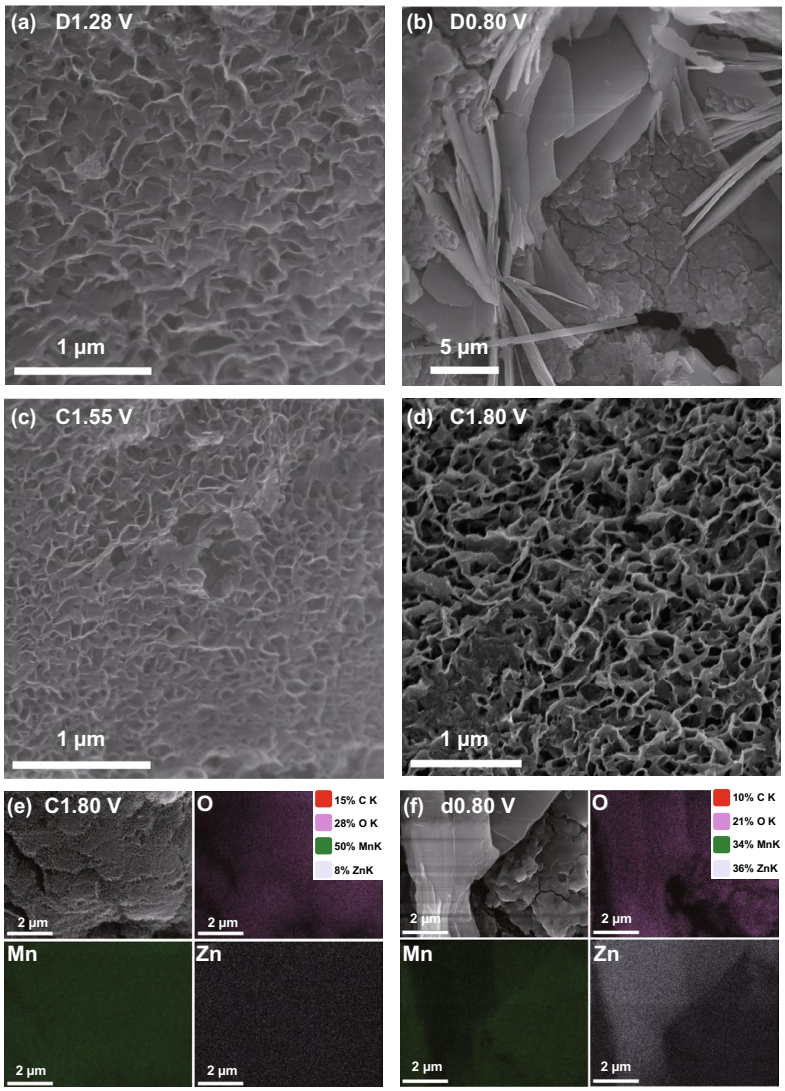


**Fig. 4** **a–d** Ex situ SEM images at different states of $MnO_x$-2 cathode. EDX elemental (Mn, O, and Zn) mapping images **e** at fully charged state and **f** at fully discharged state

contrary, at the fully discharged state, Zn element is distributed on the flake-like substance, and Mn element is also present on the electrode, which is due to the presence of unoxidized MnO in the electrode.

Figure 5a displays the ex situ XRD patterns of $MnO_x$ electrode at different charge and discharge states. First, in the fully discharged stage (0.80 V), the XRD peaks are in good agreement with $Zn_4SO_4(OH)_6{\cdot}5H_2O$ (JCPDS No. 39-0688) phase, proving that the flake-like compounds are $Zn_4SO_4(OH)_6{\cdot}5H_2O$. After charging to 1.55 V, phases of $ZnMn_2O_4$ (JCPDS No. 24-1133) and MnOOH (JCPDS No. 74-1842) are observed. But in the fully charged stage (1.80 V), both intermediate phases, $ZnMn_2O_4$ and MnOOH, evolve into low-crystallinity $MnO_2$ with birnessite structures [32]. During the subsequence discharge process, $ZnMn_2O_4$ and MnOOH diffraction peaks re-emerge when discharging to 1.28 V, indicating a good reversibility of electrode reaction. Finally, at full depth of discharge, the regeneration of $Zn_4SO_4(OH)_6{\cdot}5H_2O$ is seen in the ex situ XRD. Combined with the ex situ SEM results, the ex situ XRD patterns of $MnO_x$ electrode reveal the reversible $Mn^{2+}/Mn^{4+}$ double redox (birnessite-type $MnO_2 \leftrightarrow$ monoclinic MnOOH and spinel $ZnMn_2O_4 \leftrightarrow Mn^{2+}$ ions).

The ex situ XPS spectra at different states are collected to gain insight into the redox behaviour of $MnO_x$ electrode. Due to the overlap of Zn 3*p*, it is difficult to

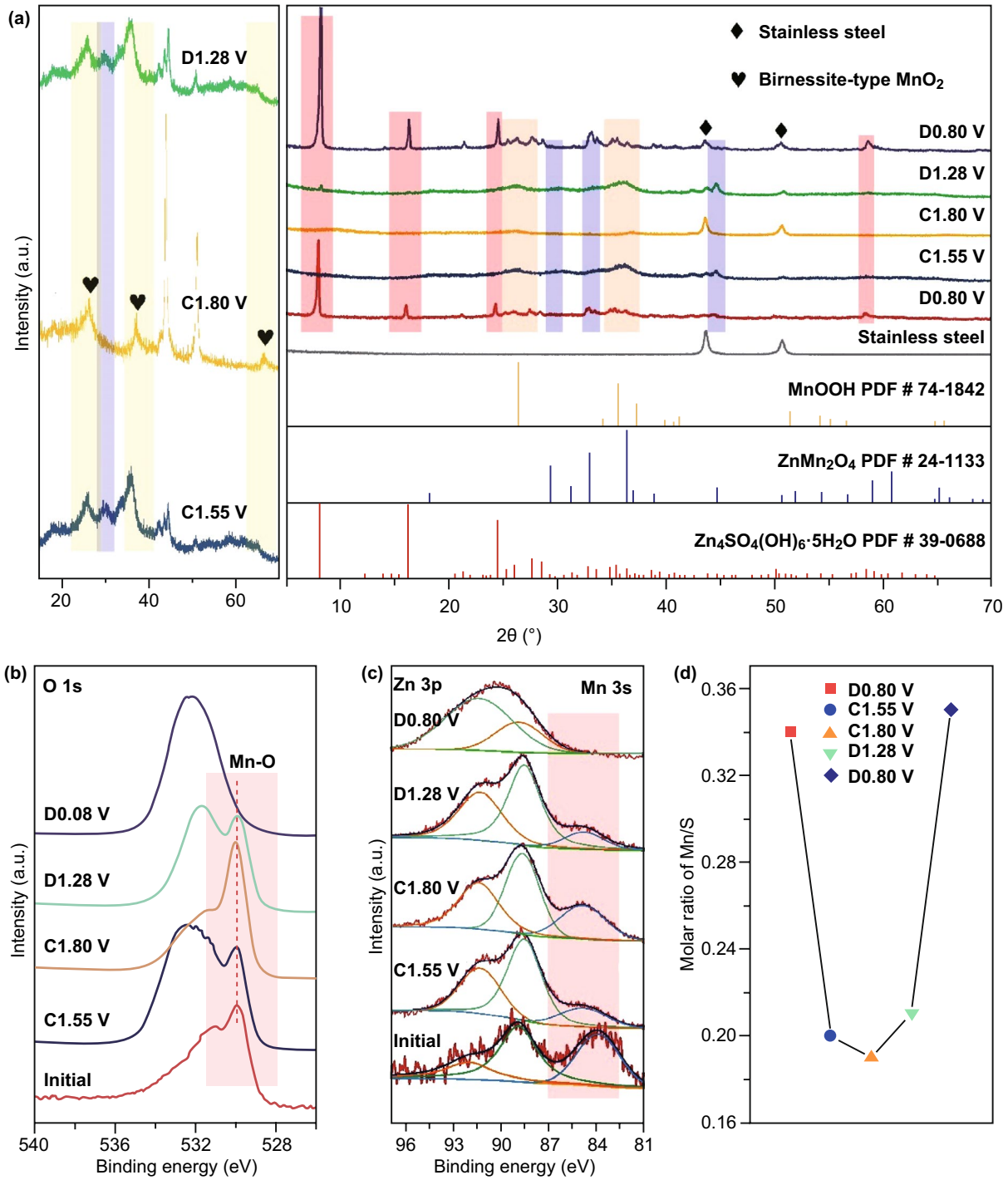


**Fig. 5** **a** Ex situ XRD patterns of the third cycle at 0.05 A $g^{-1}$ of $MnO_x$-2 cathode. XPS spectra of **b** O 1*s* and **c** Mn 3*s*/Zn 3*p* under different states of $MnO_x$-2 cathode. **d** Molar ratios of Mn/S in the electrolytes under different states of $MnO_x$-2 cathode

consistently resolve the average oxidation state of Mn at different states of charge [33]. However, it is apparent that the peak intensities of both Mn–O bond (Fig. 5b) and Mn 3*s* (Fig. 5c) increase during the charge process, and the tendency reversed during the subsequent discharge process. As shown in Fig. 5d, the molar ratios of Mn/S in the electrolyte at different stages are also analyzed by ICP-OES to strongly demonstrate the reversible $Mn^{2+}$/


https://doi.org/10.1007/s40820-020-00445-x

$Mn^{4+}$ double redox. In the fully discharged stage (0.8 V), the molar ratio of Mn/S is the highest. After charged to 1.55 V, the molar ratio of Mn/S declines precipitously. When charged to the fully charged stage (1.8 V), the molar ratio of Mn/S decreases slightly. As the electrode is discharged to 1.28 V, the molar ratio of Mn/S shows a slight rebound. After fully discharged again, a significant recovery on the molar ratio of Mn/S is observed, and the ratio is slightly higher than that of the last fully discharged state. It further supports that most of the $Mn^{2+}$ ions in the electrolyte are consumed to form the monoclinic MnOOH and spinel $ZnMn_2O_4$ phase due to the electro-oxidation process. During the following charge stages, the redox reactions between the $ZnMn_2O_4$ spinel phase (MnOOH phase) and birnessite phases cause a slight decrease of the ratio. Subsequent recovery corresponded to the dissolution of $ZnMn_2O_4$ phase and MnOOH phase into the electrolyte. Based on the above analysis, it is reasonable to conclude that manganese deposition and dissolution occurred during charge and discharge.

The cyclic voltammetry (CV) is used to further analyze the difference in electrochemical behavior between α-$MnO_2$ and $MnO_x$-2. For α-$MnO_2$ (Fig. 6a), similar to most $MnO_2$ cathodes, its open-circuit voltage is 1.36 V. The current response observed at 1.14 V is associated with the formation of monoclinic MnOOH or spinel $ZnMn_2O_4$ in the initial cathodic polarization process [34, 35]. In the initial anodic sweep, the current response observed at 1.62 V is similar to the following three scans for α-$MnO_2$ electrode, which is ascribed to the extraction process of $H^+$ or $Zn^{2+}$ [36, 37]. The reactions can be formulated as follows:

$$MnOOH \leftrightarrow MnO_2 + H^+ + e^- \quad (1)$$

$$ZnMn_2O_4 \leftrightarrow Zn^{2+} + 2MnO_2 + 2e^- \quad (2)$$

Interestingly, the $MnO_x$ cathode has a low open-circuit voltage of 0.88 V. The currents are very strong at 1.53

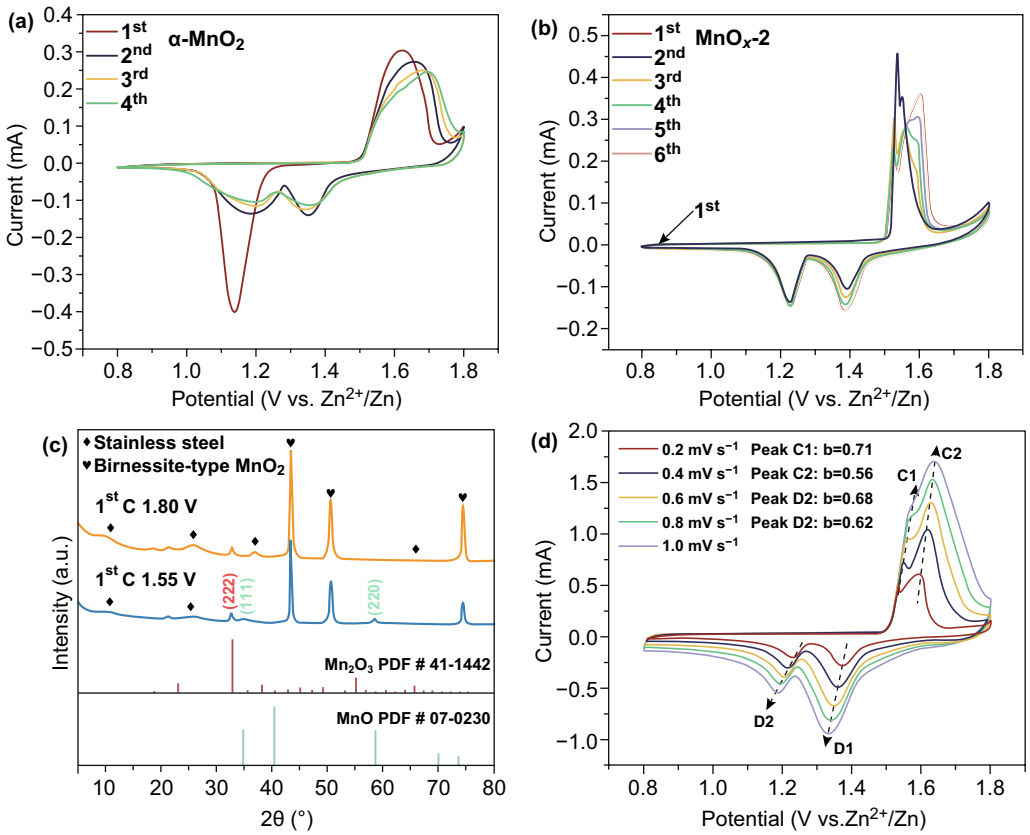


**Fig. 6** CV curves of **a** α-$MnO_2$ electrode at 0.1 mV $s^{-1}$ and **b** $MnO_x$-2 electrode at 0.1 mV $s^{-1}$. **c** Ex situ XRD patterns of the first cycle. **d** CV curves of the $MnO_x$-2 cathode at different sweep rates

and 1.55 V in the initial anodic sweep (Fig. 6b), which are related to the consequent oxidations of $Mn^{2+}$ to $Mn^{3+}$ and $Mn^{4+}$. The XRD patterns of $MnO_x$ electrode during the first charge process are shown in Fig. 6c. The patterns demonstrate the emerge of low-crystallinity birnessite-type $MnO_2$. And we propose the following possible reaction pathways:

$$3MnO \rightarrow Mn_2O_3 + Mn^{2+} + 2e^- \quad (3)$$

$$2Mn_2O_3 \rightarrow 3MnO_2 + Mn^{2+} + 2e^- \quad (4)$$

Combined with the ex situ XRD results, the two well-defined cathodic peaks at 1.23 and 1.38 V and anodic peaks near 1.52 and 1.60 V correspond to the two-step electrochemical reaction between $Mn^{2+}$ and $Mn^{4+}$. Based on the above discussions, the energy storage mechanism of $MnO_x$ electrode is described as follows:

$$2MnO_2 + Zn^{2+} + 2e^- \leftrightarrow ZnMn_2O_4 \quad (5)$$

$$MnO_2 + H^+ + e^- \leftrightarrow MnOOH \quad (6)$$

$$3ZnMn_2O_4 + 4SO_4^{2-} + 32H_2O + 13Zn^{2+} + 6e^- \leftrightarrow 6Mn^{2+} + 4Zn_4SO_4(OH)_6 \cdot 5H_2O \quad (7)$$

$$2MnOOH + SO_4^{2-} + 7H_2O + 4Zn^{2+} + 2e^- \leftrightarrow 2Mn^{2+} + Zn_4SO_4(OH)_6 \cdot 5H_2O \quad (8)$$

Apparently, stronger peak intensity is observed in $MnO_x$-2 electrode, indicating its higher electrochemical reactivity and higher capacity [38]. In addition, the overpotential gaps of $MnO_x$-2 electrode are smaller than that of α-$MnO_2$ electrode. The higher reactivity and smaller polarization of $MnO_x$-2 may be caused by the low crystallinity of in situ generated birnessite-type $MnO_2$.

As shown in Fig. 6d, the CV curves of the $MnO_x$ at different scanning rates are further used to determine the electrochemical behavior. In general, the peak current ($i$) obeys an empirical power-law relationship with the scan rate ($v$):

$$i = av^b \quad (9)$$

$$\log(i) = b\log(v) + \log(a) \quad (10)$$

The parameter $b$ determined by the plots of log ($i$) and log ($\nu$) reflects the dominated diffusion modes [39, 40]. And the parameter $b$ for both anodic and cathodic peaks is calculated to be 0.71, 0.56, 0.68, and 0.62, respectively. The $b$-value of the four peaks is close to 0.5, demonstrating that the conversion reaction and the insertion/extraction of $H^+$ and $Zn^{2+}$ are controlled by diffusion.

## 4 Conclusions

In summary, a rechargeable aqueous zinc–manganese battery with promising electrochemical performance is developed. The low-crystallinity birnessite-type $MnO_2$ generated in situ from carbon-coated $MnO_x$ nanoparticles achieves the reversible $Mn^{2+}/Mn^{4+}$ double redox. The mechanism involves a reversible double redox between $Mn^{2+}$ and birnessite-type $MnO_2$. Benefitting from the reversible $Mn^{2+}/Mn^{4+}$ double redox, the $MnO_x$ cathode using $Mn^{2+}$-containing $ZnSO_4$ electrolyte exhibits excellent electrochemical properties with superior cycling stability and high capacity in comparison with most of the reported cathodes for AZIBs. The analysis of electrochemical reaction mechanism will open a promising avenue to further enhance the energy density of aqueous batteries. The overall combination of low-cost $MnO_x$ cathode materials, mild aqueous electrolytes, metal Zn anode, and simpler assembly parameters can allow aqueous zinc–manganese batteries meet the requirements of large-scale storage applications.

**Acknowledgements** This work is supported by the National Natural Science Foundation of China (Grant No. 51772331) and the National Key Technologies R&D Program (Grant No. 2018YFB1106000).



**Electronic supplementary material** The online version of this article (https://doi.org/10.1007/s40820-020-00445-x) contains supplementary material, which is available to authorized users.

## References


1. M. Armand, J.-M. Tarascon, Building better batteries. Nature **451**, 652–657 (2008). https://doi.org/10.1038/451652a
2. J.B. Goodenough, Electrochemical energy storage in a sustainable modern society. Energy Environ. Sci. **7**, 14–18 (2014). https://doi.org/10.1039/C3EE42613K
3. M.S. Whittingham, Lithium batteries and cathode materials. Chem. Rev. **104**, 4271–4302 (2004). https://doi.org/10.1021/cr020731c
4. E.A. Olivetti, G. Ceder, G.G. Gaustad, X. Fu, Lithium-ion battery supply chain considerations: analysis of potential bottlenecks in critical metals. Joule **1**, 229–243 (2017). https://doi.org/10.1016/j.joule.2017.08.019
5. S. Chu, A. Majumdar, Opportunities and challenges for a sustainable energy future. Nature **448**, 294–303 (2012). https://doi.org/10.1038/nature11475
6. N. Nitta, F. Wu, J.T. Lee, G. Yushin, Li-ion battery materials: present and future. Mater. Today **18**, 252–264 (2015). https://doi.org/10.1016/j.mattod.2014.10.040
7. F. Wan, L. Zhang, X. Dai, X. Wang, Z. Niu, J. Chen, Aqueous rechargeable zinc/sodium vanadate batteries with enhanced performance from simultaneous insertion of dual carriers. Nat. Commun. **9**, 1656 (2018). https://doi.org/10.1038/s41467-018-04060-8
8. F. Wan, Y. Zhang, L. Zhang, D. Liu, C. Wang, L. Song, Z. Niu, J. Chen, Reversible oxygen redox chemistry in aqueous zinc-ion batteries. Angew. Chem. Int. Ed. **58**, 7062–7067 (2019). https://doi.org/10.1002/anie.201902679
9. C. Xu, B. Li, H. Du, F. Kang, Energetic zinc ion chemistry: the rechargeable zinc ion battery. Angew. Chem. Int. Ed. **51**, 933–935 (2012). https://doi.org/10.1002/anie.201106307
10. M. Chamoun, W.R. Brant, C.-W. Tai, G. Karlsson, D. Noréus, Rechargeability of aqueous sulfate Zn/$MnO_2$ batteries enhanced by accessible $Mn^{2+}$ ions. Energy Storage Mater. **15**, 351–360 (2018). https://doi.org/10.1016/j.ensm.2018.06.019
11. B. Wu, G. Zhang, M. Yan, T. Xiong, P. He, L. He, X. Xu, L. Mai, Graphene scroll-coated α-$MnO_2$ nanowires as high-performance cathode materials for aqueous Zn-Ion battery. Small **14**, 1703850 (2018). https://doi.org/10.1002/smll.201703850
12. H. Li, C. Han, Y. Huang, M. Zhu, Z. Pei et al., An extremely safe and wearable solid-state zinc ion battery based on a hierarchical structured polymer electrolyte. Energy Environ. Sci. **11**, 941–951 (2018). https://doi.org/10.1039/C7EE03232C
13. N. Zhang, F. Cheng, J. Liu, L. Wang, X. Long, X. Liu, F. Li, J. Chen, Rechargeable aqueous zinc-manganese dioxide batteries with high energy and power densities. Nat. Commun. **8**, 405 (2017). https://doi.org/10.1038/s41467-017-00467-x
14. N. Qiu, H. Chen, Z. Yang, S. Sun, Y. Wang, Low-cost birnessite as a promising cathode for high-performance aqueous rechargeable batteries. Electrochim. Acta **272**, 154–160 (2018). https://doi.org/10.1016/j.electacta.2018.04.012
15. Y. Zeng, X. Zhang, Y. Meng, M. Yu, J. Yi, Y. Wu, X. Lu, Y. Tong, Achieving ultrahigh energy density and long durability in a flexible rechargeable quasi-solid-state Zn-$MnO_2$ battery. Adv. Mater. **29**, 1700274 (2017). https://doi.org/10.1002/adma.201700274
16. M. Song, H. Tan, D. Chao, H.J. Fan, Recent advances in Zn-Ion batteries. Adv. Funct. Mater. **28**, 1802564 (2018). https://doi.org/10.1002/adfm.201802564
17. N. Zhang, F. Cheng, Y. Liu, Q. Zhao, K. Lei, C. Chen, X. Liu, J. Chen, Cation-deficient spinel $ZnMn_2O_4$ cathode in $Zn(CF_3SO_3)_2$ electrolyte for rechargeable aqueous Zn-ion battery. J. Am. Chem. Soc. **138**, 12894–12901 (2016). https://doi.org/10.1021/jacs.6b05958
18. X. Wu, Y. Xiang, Q. Peng, X. Wu, Y. Li et al., Green-low-cost rechargeable aqueous zinc-ion batteries using hollow porous spinel $ZnMn_2O_4$ as the cathode material. J. Mater. Chem. A **5**, 17990–17997 (2017). https://doi.org/10.1039/C7TA00100B
19. J. Hao, J. Mou, J. Zhang, L. Dong, W. Liu, C. Xu, F. Kang, Electrochemically induced spinel-layered phase transition of $Mn_3O_4$ in high performance neutral aqueous rechargeable zinc battery. Electrochim. Acta **259**, 170–178 (2018). https://doi.org/10.1016/j.electacta.2017.10.166
20. Y. Fu, Q. Wei, G. Zhang, X. Wang, J. Zhang et al., Electrochemically induced spinel-layered phase transition of $Mn_3O_4$ in high performance neutral aqueous rechargeable zinc battery. Electrochim. Acta **8**, 1801445 (2018). https://doi.org/10.1016/j.electacta.2017.10.166
21. J. Ming, J. Guo, C. Xia, W. Wang, H.N. Alshareef, Zinc-ion batteries: materials, mechanisms, and applications. Mater. Sci. Eng. R **135**, 58–84 (2019). https://doi.org/10.1016/j.mser.2018.10.002
22. M.H. Alfaruqi, V. Mathew, J. Gim, S. Kim, J. Song, J. Baboo, S. Choi, J. Kim, Electrochemically induced structural transformation in a γ-$MnO_2$ cathode of a high capacity zinc-ion battery system. Chem. Mater. **27**, 3609–3620 (2015). https://doi.org/10.1021/cm504717p
23. W. Sun, F. Wang, S. Hou, C. Yang, X. Fan et al., Zn/$MnO_2$ battery chemistry With $H^+$ and $Zn^{2+}$ coinsertion. J. Am. Chem. Soc. **139**, 9775–9778 (2017). https://doi.org/10.1021/jacs.7b04471
24. A.V. Radha, T.Z. Forbes, C.E. Killian, P.U.P.A. Gilbert, A. Navrotsky, Transformation and crystallization energetics of synthetic and biogenic amorphous calcium carbonate. Proc. Natl. Acad. Sci. USA **107**, 16438–16443 (2010). https://doi.org/10.1073/pnas.1009959107
25. W. Chen, R.B. Rakhia, H.N. Alshareef, Facile synthesis of polyaniline nanotubes using reactive oxide templates for high energy density pseudocapacitors. J. Mater. Chem. A **1**, 3315–3324 (2013). https://doi.org/10.1039/c3ta00499f
26. V. Di Castro, G. Polzonetti, XPS study of MnO oxidation. J. Electron. Spectrosc. **48**, 117–123 (1989). https://doi.org/10.1016/0368-2048(89)80009-X
27. M. Zhong, D. Yang, C. Xie, Z. Zhang, Z. Zhou, X.H. Bu, Yolk–shell MnO@$ZnMn_2O_4$/N–C nanorods derived from α-$MnO_2$/ZIF-8 as anode materials for lithium ion batteries.

Small **12**, 5564 (2016). https://doi.org/10.1002/smll.201601959

28. D. Kang, Q. Liu, R. Si, J. Gu, W. Zhang, D. Zhang, Crosslinking-derived MnO/carbon hybrid with ultrasmall nanoparticles for increasing lithium storage capacity during cycling. Carbon **99**, 138–147 (2016). https://doi.org/10.1016/j.carbon.2015.11.068
29. Y. Fu, Q. Wei, G. Zhang, X. Wang, J. Zhang et al., High-performance reversible aqueous Zn-ion battery based on porous $MnO_x$ nanorods coated by MOF-derived N-doped carbon. Adv. Energy Mater. **8**, 1801445 (2018). https://doi.org/10.1002/aenm.201801445
30. J. Liu, S. Tang, Y. Lu, G. Cai, S. Liang, W. Wang, X. Chen, Synthesis of $Mo_2N$ nanolayer coated $MoO_2$ hollow nanostructures as high-performance anode materials for lithium-ion batteries. Energy Environ. Sci. **6**, 2691–2697 (2013). https://doi.org/10.1039/c3ee41006d
31. T. Xiong, Z.G. Yu, H. Wu, Y. Du, Q. Xie et al., Defect engineering of oxygen-deficient manganese oxide to achieve high-performing aqueous zinc ion battery. Adv. Energy Mater. **9**, 1803815 (2019). https://doi.org/10.1002/aenm.201803815
32. S. Zhao, B. Han, D. Zhang, Q. Huang, L. Xiao et al., Unravelling the reaction chemistry and degradation mechanism in aqueous Zn/$MnO_2$ rechargeable batteries. J. Mater. Chem. A **6**, 5733–5739 (2018). https://doi.org/10.1039/C8TA01031E
33. X. Yang, Y. Makita, Z. Liu, K. Sakane, K. Ooi, Structural characterization of self-assembled $MnO_2$ nanosheets from birnessite manganese oxide single crystals. Chem. Mater. **16**, 5581–5588 (2004). https://doi.org/10.1021/cm049025d
34. H. Pan, Y. Shao, P. Yan, Y. Cheng, K. Han et al., Reversible aqueous zinc/manganese oxide energy storage from conversion reactions. Nat. Energy **1**, 16039 (2016). https://doi.org/10.1038/nenergy.2016.39
35. Y. Li, S. Wang, J.R. Salvador, J. Wu, B. Liu et al., Reaction mechanisms for long-life rechargeable Zn/$MnO_2$ batteries. Chem. Mater. **31**, 2036–2047 (2019). https://doi.org/10.1021/acs.chemmater.8b05093
36. B. Lee, H.R. Lee, H. Kim, K.Y. Chung, B.W. Cho, S.H. Oh, Elucidating the intercalation mechanism of zinc ions into α-$MnO_2$ for rechargeable zinc batteries. Chem. Commun. **51**, 9265–9268 (2015). https://doi.org/10.1039/C5CC02585K
37. B. Lee, H.R. Seo, H.R. Lee, C.S. Yoon, J.H. Kim, K.Y. Chung, B.W. Cho, S.H. Oh, Critical role of pH evolution of electrolyte in the reaction mechanism for rechargeable zinc batteries. Chemsuschem **9**, 2948–2956 (2016). https://doi.org/10.1002/cssc.201600702
38. Y. Zhang, Z. Ding, C. Foster, C. Banks, X. Qiu, X. Ji, Oxygen vacancies evoked blue $TiO_2$(B) nanobelts with efficiency enhancement in sodium storage behaviors. Adv. Funct. Mater. **27**, 1700856 (2017). https://doi.org/10.1002/adfm.201700856
39. D. Chao, C. Zhu, P. Yang, X. Xia, J. Liu et al., Array of nanosheets render ultrafast and high-capacity Na-ion storage by tunable pseudocapacitance. Nat. Commun. **7**, 12122 (2016). https://doi.org/10.1038/ncomms12122
40. D. Chao, P. Liang, Z. Chen, L. Bai, H. Shen et al., Pseudocapacitive Na-ion storage boosts high rate and areal capacity of self-branched 2D layered metal chalcogenide nanoarrays. ACS Nano **10**, 10211–10219 (2016). https://doi.org/10.1021/acsnano.6b05566

 https://doi.org/10.1007/s40820-020-00445-x